Inorganic Chemistry
Cite This: Inorg. Chem. 2019, 58, 8245−8252
Article
pubs.acs.org/IC

Dual-Mode Optical Thermometry Based on the Fluorescence Intensity Ratio Excited by a 915 nm Wavelength in $LuVO_4$:Yb^{3+}/Er^{3+}@SiO_2 Nanoparticles

Guotao Xiang,*[,†] Xiaotong Liu,[†] Jiahua Zhang,[‡] Zhen Liu,[†] Wen Liu,[§] Yan Ma,[†] Sha Jiang,[†] Xiao Tang,[†] Xianju Zhou,[†] Li Li,[†] and Ye Jin[∥]

[†]Department of Mathematics and Physics, Chongqing University of Posts and Telecommunications, 2 Chongwen Road, Chongqing 400065, China

[‡]State Key Laboratory of Luminescence and Applications, Changchun Institute of Optics, Fine Mechanics and Physics, Chinese Academy of Sciences, 3888 Eastern South Lake Road, Changchun 130033, China

[§]College of Physics, Liaoning University, 66 Chongshan Middle Road, Shenyang 110036, China

[∥]School of Science, Chongqing University of Technology, 69 Hongguang Street, Chongqing 400054, China

Supporting Information

ABSTRACT: The optical thermometry properties of $LuVO_4$:Yb^{3+}/Er^{3+}@SiO_2 nanoparticles (NPs) are studied in detail. In order to avoid the overheating effect for biological tissue caused by 980 nm radiation, 915 nm is employed as the excitation wavelength to investigate the upconversion (UC) and optical thermometry properties of the as-prepared NPs. In the visible region, the fluorescence intensity ratio (FIR) of the $^2H_{11/2}$ and $^4S_{3/2}$ levels of Er^{3+} is utilized to measure the temperature. The relative sensitivity S_R in this case can be written as $1077/T^2$, which is higher than that of β-$NaYF_4$:Yb^{3+}/Er^{3+} NPs, β-$NaLuF_4$:Yb^{3+}/Er^{3+} NPs, YVO_4:Yb^{3+}/Er^{3+} NPs, etc. In the near-infrared (NIR) region, an anomalous enhancement of the $^4I_{13/2} \rightarrow {}^4I_{15/2}$ transition with increasing temperature is observed. What is more, the FIR of peak 2 (located at 1496 nm) to peak 1 (located at 1527 nm) is changed regularly with increasing temperature, which can also be used to measure the temperature. The combination of the visible and NIR regions for optical thermometry can provide a self-referenced temperature determination to make measurement of the temperature more precise. In addition, the UC mechanism is also investigated, especially the population route of the $^4F_{9/2}$ level of Er^{3+}. Through analysis of the decay curves, we propose that the dominant way for populating the Er^{3+} $^4F_{9/2}$ level is energy transfer from the Yb^{3+} $^2F_{5/2}$ level to the Er^{3+} $^4I_{13/2}$ level. All of the results reveal the potential application of $LuVO_4$:Yb^{3+}/Er^{3+}@SiO_2 NPs for dual-mode optical thermometry.

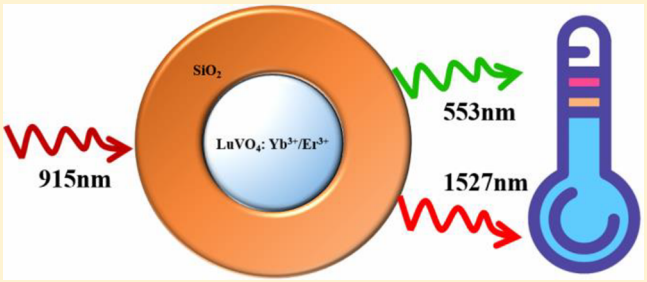

INTRODUCTION

Accurate and fast temperature measurement is of great significance in every area, such as medical treatments, oil refineries, coal mines, and so on. Among the various methods for temperature detection, optical thermometry is a promising research owing to its tremendous advantages in terms of rapid response, noncontact, and strong antijamming capability.[1−7] Currently, rare-earth-ion-doped inorganic materials, especially upconversion (UC) nanomaterials, have become a research hotspot for optical thermometry.[8−10] Compared with the fluorescence temperature-sensing materials based on quantum dots and organic dyes, UC materials have many excellent properties, such as strong photostability, high resolution, negligible autofluorescence background, low toxicity, etc.[11,12] Meanwhile, UC materials also show great potential applications in photodynamic therapy (PDT) and photothermal therapy (PTT).[13,14] Therefore, developing UC nanomaterials may be a promising way to combine PDT or PTT with optical thermometry for biomedicine to provide a real-time temperature detection during the treatment process.

In general, 980 nm is usually chosen as the excitation wavelength to trigger UC luminescence because of the sensitizer Yb^{3+} ions' excellent absorption capacity at this wavelength. However, it is necessary to point out that water and biological tissue have extremely strong optical absorption from 930 to 1030 nm.[15] That means that 980 nm radiation would cause a serious overheating effect, resulting in biological tissue injury. At present, to overcome this drawback, 808 and 915 nm are employed as the excitation wavelengths for UC luminescence. To utilize 808 nm as the excitation wavelength, Nd^{3+} is often chosen as the sensitizer and a complex core−

Received: April 26, 2019
Published: May 30, 2019

DOI: 10.1021/acs.inorgchem.9b01229
Inorg. Chem. 2019, 58, 8245−8252

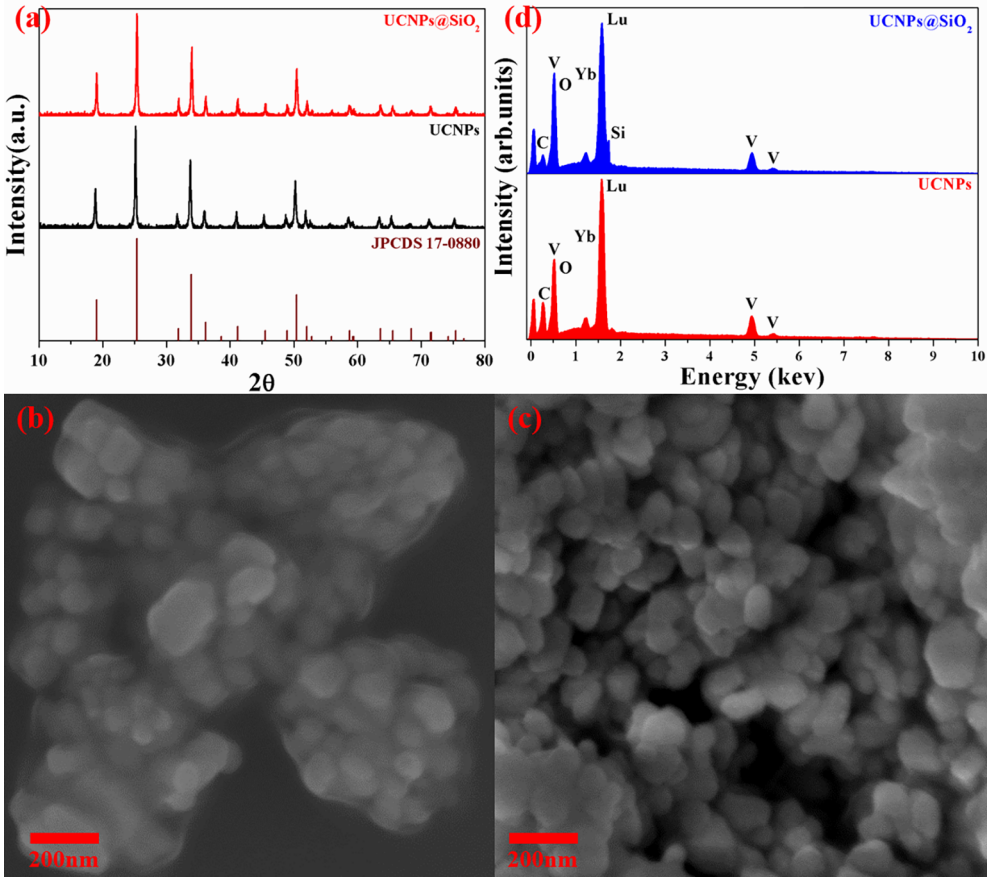

Figure 1. (a) XRD data of UCNPs and UCNPs@SiO_2 along with the standard XRD data of $LuVO_4$ (JCPDS 17-0880). SEM images of (b) UCNPs and (c) UCNPs@SiO_2. (d) EDS spectra of UCNPs and UCNPs@SiO_2.

shell−shell structure is necessary to avoid luminescence quenching.[16,17] Using 915 nm as the excitation wavelength, by contrast, is more easily realized, which is still based on Yb^{3+} sensitizing.[18,19] Nevertheless, because the optical absorption capacity of Yb^{3+} ions at 915 nm is only half that at 980 nm, the intensity of UC under 915-nm-wavelength excitation is weaker than that under 980-nm-wavelength excitation.[19] Therefore, considering that the intense UC emission is required for accurate temperature measurement, there is an urgent need to develop the UC materials with high efficiency under 915-nm-wavelength excitation.

Rare-earth vanadate, which owns low photon energy and excellent electrooptical properties, is one kind of promising matrix for highly efficient UC luminescence. For example, Cheng et al. and Oh et al. have reported strong UC in $YVO_4:Yb^{3+}/Er^{3+}$ and $GdVO_4:Yb^{3+}/Er^{3+}$, respectively.[20,21] However, the luminescence properties of $LuVO_4$, which is another representative rare-earth vanadate, are seldom studied, particularly its UC properties and temperature-sensing behaviors, under 915-nm-wavelength excitation.

Herein, a hydrothermal method was used to synthesize the $LuVO_4:Yb^{3+}/Er^{3+}$ nanoparticles (NPs) and $LuVO_4:Yb^{3+}/Er^{3+}$@SiO_2 NPs. Excited by a 915 nm wavelength, the optical thermometry properties based on the fluorescence intensity ratio (FIR) of the Er^{3+} $^2H_{11/2}$ level to the $^4S_{3/2}$ level and peak 2 (at 1496 nm) to peak 1 (at 1527 nm) of the Er^{3+} $^4I_{13/2} \rightarrow {}^4I_{15/2}$ transition have been studied in detail. The two methods for optical thermometry can be utilized simultaneously, which allows for a self-referenced temperature determination to make measurement of the temperature more precise. In addition, the UC mechanism is also investigated, especially the population route of the $^4F_{9/2}$ level of Er^{3+} ions. All of the results indicate the potential application of $LuVO_4:Yb^{3+}/Er^{3+}$@SiO_2 NPs for dual-mode optical thermometry.

EXPERIMENTAL SECTION

Materials. Lu_2O_3 (99.99%), Yb_2O_3 (99.99%), and Er_2O_3 (99.99%) were supplied by Beijing Founde Star Science & Technology Co, Ltd. NH_4OH (analytical grade) and NH_4VO_3 (analytical grade) were purchased from Chongqing Chuandong Chemical (Group) Co., Ltd. Tetraacetoxysilane [$Si(OC_2H_5)_4$, TEOS, 99%] was supplied by Alfa-Aesar. The chemical reagents in this work were used as the raw materials without further refinement.

Synthesis of $LuVO_4:Yb^{3+}/Er^{3+}$ NPs. $LuVO_4$:20 mol % Yb^{3+}/2 mol % Er^{3+} NPs (UCNPs) were prepared by a hydrothermal process. Details of the preparation process are as follows: First, the rare-earth oxides (Lu_2O_3, Yb_2O_3, and Er_2O_3) with the required molar ratio were dissolved in a diluted nitric acid solution with continuous heating and stirring to obtain the rare-earth nitrate solution, in which the pH value was adjusted to 6 by adding deionized water. Subsequently, a water solution containing 4 mmol of NH_4VO_3 was added into the rare-earth nitrate solution to obtain a 40 mL mixture solution. Finally, the pH value of the mixture solution was adjusted to 7 by the addition of NH_4OH with continuous stirring for 1 h. Then, the clear yellow solution was transferred to a 75 mL sealed Teflon-lined autoclave and heated at 185 °C for 24 h. The resultant products were collected by centrifugation, washed with ethanol, and dried at 120 °C in an air atmosphere. In addition, to enhance the UC intensity of the samples, the NPs were then annealed at 600 °C for 5 h in a muffle furnace.

Synthesis of $LuVO_4:Yb^{3+}/Er^{3+}$@SiO_2 NPs. On the basis of the above experiments, the as-prepared $LuVO_4$:20 mol % Yb^{3+}/2 mol %

DOI: 10.1021/acs.inorgchem.9b01229
Inorg. Chem. 2019, 58, 8245−8252

Er^{3+} NPs were used as the raw materials and TEOS was used to catalyze alkali hydrolysis. First, half of the prepared $LuVO_4$:Yb^{3+}/Er^{3+} NPs were dissolved in 40 mL of ethanol and 4 mL of deionized water, in which the pH value was adjusted to 9 by adding NH_4OH. Then, 2 mL of TEOS was dropped into the solution with continuous stirring for 4 h. Finally, the products were collected by centrifugation, cleaned by ethanol, and dried at 120 °C to obtain $LuVO_4$:Yb^{3+}/Er^{3+}@SiO_2 NPs (UCNPs@SiO_2).

Characterization. A Bruker D8 Advance diffractometer was used to collect the X-ray diffraction (XRD) data of the as-prepared samples. The morphology and chemical analysis of the NPs were measured by microscopy (Hitachi S-4800) coupled with energy-dispersive X-ray spectrometry (EDS). The UC and NIR emission spectra were obtained by using an Edinburgh FLS920 spectrometer. When an optical parametric oscillator was used as the excitation source, the decay curves were recorded by a TDS-3052 oscilloscope purchased from Tektronix. The lifetimes of the NPs were obtained by integrating the area of the corresponding normalized decay curves.

RESULTS AND DISCUSSION

Structure. The XRD data of UCNPs and UCNPs@SiO_2 were measured and are depicted in Figure 1a. It can be clearly seen that the two samples present similar XRD patterns and the peaks of each sample match well with the tetragonal phase $LuVO_4$ standard data (JCPDS 17-0880). No other phases can be detected. The scanning electron microscopy (SEM) images of the as-prepared samples are shown in parts b and c of Figure 1, respectively. The average sizes of UCNPs and UCNPs@SiO_2 are 85 and 91 nm, respectively, indicating that the thickness of the coating SiO_2 layer is about 3 nm around the NPs. Moreover, the EDS spectra of UCNPs and UCNPs@SiO_2 were also measured to further prove the core−shell structure (see Figure 1d). Compared with UCNPs, the peak for Si was only observed in UCNPs@SiO_2, suggesting the successful coating of the SiO_2 shell.

Luminescence Properties. *UC Luminescence of UCNPs and UCNPs@SiO_2.* Figure 2a depicts the normalized UC spectra of UCNPs@SiO_2 dispersed in water excited by 915 and 980 nm wavelengths, respectively. Before collection of the spectral data, the sample was irradiated persistently by 915 and 980 nm near-infrared (NIR) light for 3 min, respectively. Meanwhile, the excitation power density of the 980 nm wavelength remained the same as that of the 915 nm wavelength. Obviously, the intensity ratio of the $^2H_{11/2} \rightarrow {}^4I_{15/2}$ transition to the $^4S_{3/2} \rightarrow {}^4I_{15/2}$ transition is increased when the excitation wavelength is changed from 915 to 980 nm, resulting from the absorption effect of the 980 nm wavelength by water, which caused increasing temperature of the sample. Actually, because $^2H_{11/2}$ and $^4S_{3/2}$ are thermally coupled levels, the Er^{3+} $^2H_{11/2}$ state can be populated from the Er^{3+} $^4S_{3/2}$ state through a thermal excitation effect at higher temperature. From this, it can be proven that the absorption effect of the 980 nm wavelength by water is stronger than that of the 915 nm wavelength. Therefore, in a subsequent article, 915 nm is employed as the excitation wavelength to trigger UC luminescence.

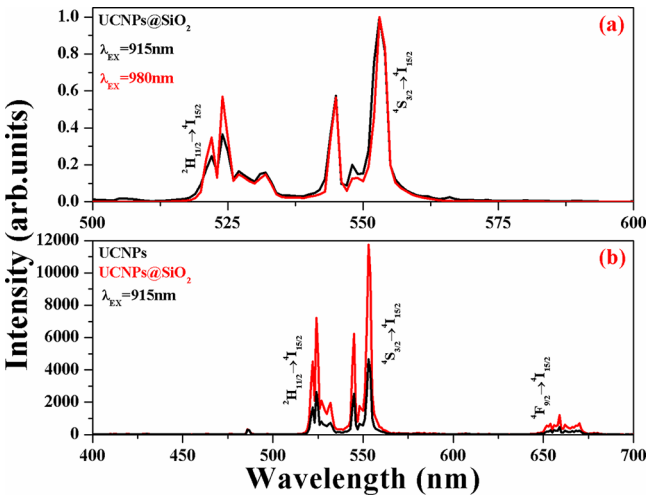

Figure 2. (a) Normalized UC spectra of UCNPs@SiO_2 dispersed in water excited by 915 and 980 nm with the same power density. (b) UC spectra of UCNPs and UCNPs@SiO_2 excited by a 915 nm wavelength.

Next, in order to explore the effect of the core−shell structure on the UC emission intensity, the UC spectra of UCNPs and UCNPs@SiO_2 under 915-nm-wavelength excitation were measured and are depicted in Figure 2b. Definitely, the UC intensity is dramatically enhanced by coating the SiO_2 shell with a factor of approximately 2.5 times for both the $^2H_{11/2}/{}^4S_{3/2} \rightarrow {}^4I_{15/2}$ transition (green emission) and the $^4F_{9/2} \rightarrow {}^4I_{15/2}$ transition (red emission). Actually, in the past few years, there are many papers in the literature concerning UC enhancement realized by coating SiO_2 on the surface of NPs.[22−24] Overall, the UC intensity enhancement by coating SiO_2 can be ascribed to two aspects: the increase of light extraction from the inside of the NPs and the decrease of energy transfer (ET) from the luminescence centers to surface defects. To be specific, as is known to all, when light travels from an optically dense medium (refractive index named n_{r2}) to an optically thinner medium (refractive index named n_{r1}), if the incidence angle (θ) is larger than the critical value [$\theta_C = \arcsin(n_{r1}/n_{r2})$], a total internal reflection phenomenon at the interface should occur. The refractive index of SiO_2 is reported to be about 1.46 (n_S), which is much smaller than that of $LuVO_4$ (n_L = 2.03). In UCNPs, the critical angle θ_{C0} for Er^{3+} emitting visible light from the inside of the NPs to air (n = 1) is about 30°. However, in UCNPs@SiO_2, a much larger critical angle can be obtained by introducing a mediated layer of SiO_2 between the NPs and air, at the interface of either the NPs and SiO_2 (θ_{C1} = 46°) or SiO_2 and air (θ_{C2} = 43°), which means that the NPs with surface treatment by SiO_2 should have more light extraction than that of the bare NPs. Therefore, this is proposed to be one of the reasons for UC enhancement through SiO_2 coating.[25,26] In addition, after coating SiO_2 on the surface of UCNPs, the distance between the luminescence centers and the new surface supplied by SiO_2 is increased, which can effectively reduce the ET process from the luminescence centers to the defects on the particles' surface, resulting in UC enhancement.[26,27]

In order to acquire more information about the UC process, the dependence of the UC intensity on the pump power of a 915-nm-wavelength excitation is measured. As is known to all, the UC intensity I is proportional to P^n in a multiphoton process: $I = P^n$, where P represents the NIR excitation power and n is the number of required NIR photons for emitting one visible photon, which can be calculated by the slope of the double-logarithmic plots between I and P. As shown in Figure 3, the n values of the $^2H_{11/2}/{}^4S_{3/2} \rightarrow {}^4I_{15/2}$ transition (green UC emission) and the $^4F_{9/2} \rightarrow {}^4I_{15/2}$ transition (red UC emission) in UCNPs are 1.6 and 1.5, respectively, revealing a two-photon process for both of the transitions. The same result appears in UCNPs@SiO_2.

DOI: 10.1021/acs.inorgchem.9b01229
Inorg. Chem. 2019, 58, 8245−8252

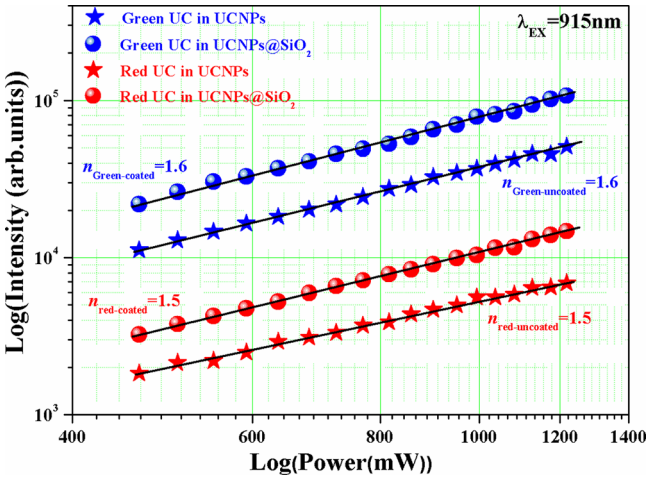

Figure 3. Pump power dependence of the integrated UC intensity of UCNPs and UCNPs@SiO_2 excited by a 915 nm wavelength.

On the basis of the above analysis, the possible ET processes excited by a 915 nm wavelength are depicted in Figure 4.

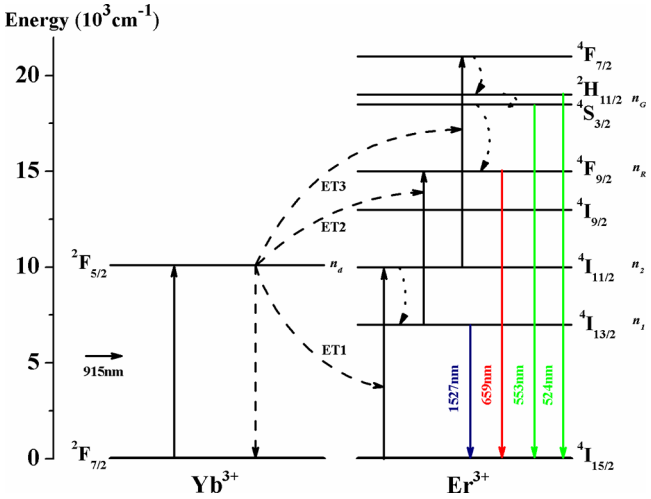

Figure 4. Energy-level diagram with the possible ET processes excited by a 915 nm wavelength.

Under a 915-nm-wavelength excitation, the Yb^{3+} ions can be populated to the $^2F_{5/2}$ level from the ground state. The main route for populating the green UC emission level Er^{3+} $^2H_{11/2}/^4S_{3/2}$ includes ET1 from the Yb^{3+} $^2F_{5/2}$ level to the ground state of Er^{3+} and ET3 from the Yb^{3+} $^2F_{5/2}$ level to the Er^{3+} $^4I_{11/2}$ level along with a multiphonon relaxation process (MPR) from the Er^{3+} $^4F_{7/2}$ level. For the red UC emission level Er^{3+} $^4F_{9/2}$, it can be populated by the ET2 process from the Yb^{3+} $^2F_{5/2}$ level to the Er^{3+} $^4I_{13/2}$ level. Moreover, the MPR process from the Er^{3+} $^2H_{11/2}/^4S_{3/2}$ level can also populate the Er^{3+} $^4F_{9/2}$ level. In the following paragraph, the decay curves of the $^2H_{11/2}/^4S_{3/2}$ and $^4F_{9/2}$ levels of Er^{3+} were used to analyze which route is dominant for populating the $^4F_{9/2}$ level.

Parts a and b of Figure 5 show the decay curves of the $^2H_{11/2}/^4S_{3/2}$ and $^4F_{9/2}$ states of Er^{3+} under 915-nm-wavelength excitation. Definitely, the core−shell structure has almost no influence on the decay time of the two energy levels, whereas an interesting phenomenon can be observed: the decay time of the Er^{3+} $^2H_{11/2}/^4S_{3/2}$ state is approximately half that of the Er^{3+}

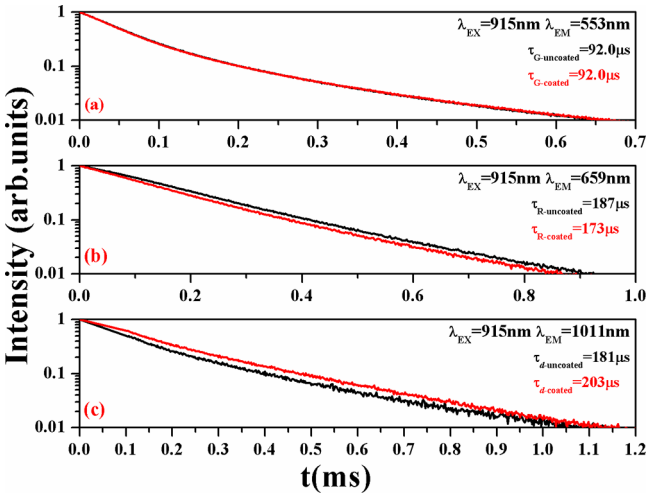

Figure 5. Decay curves of the (a) $^2H_{11/2}/^4S_{3/2}$ state of Er^{3+}, (b) $^4F_{9/2}$ state of Er^{3+}, and (c) $^2F_{5/2}$ state of Yb^{3+} under 915-nm-wavelength excitation in UCNPs and UCNPs@SiO_2, respectively.

$^4F_{9/2}$ state in each sample. Assuming that the MPR process from the $^2H_{11/2}/^4S_{3/2}$ state is dominant for populating the $^4F_{9/2}$ state, the decay time of the $^4F_{9/2}$ state should be almost equal to that of the $^2H_{11/2}/^4S_{3/2}$ state because of the rapid MPR process between the two states. Obviously, this hypothesis is inconsistent with the test data, which means that the ET2 process may be the dominant way to populate the $^4F_{9/2}$ state. Actually, the population of the $^2F_{5/2}$ state of Yb^{3+} n_d can be written as

$$n_d = n_{d0} \exp(-t/\tau_d) \quad (1)$$

the population of the $^4I_{13/2}$ state of Er^{3+} n_1 can be written as

$$n_1 = n_{10} \exp(-t/\tau_1) \quad (2)$$

and the population of the $^4I_{11/2}$ state of Er^{3+} n_2 can be written as

$$n_2 = n_{20} \exp(-t/\tau_2) \quad (3)$$

where τ_d, τ_1, and τ_2 represent the decay times of the Yb^{3+} $^2F_{5/2}$, Er^{3+} $^4I_{13/2}$, and Er^{3+} $^4I_{11/2}$ states, respectively. Subsequently, the population of the $^2H_{11/2}/^4S_{3/2}$ state n_G through ET1 and ET3 can be expressed as

$$n_G = C_{d2} n_d n_2 = C_{d2} n_{d0} n_{20} \exp[-t(1/\tau_d + 1/\tau_2)] \quad (4)$$

where C_{d2} is the coefficient for ET from the $^2F_{5/2}$ state of Yb^{3+} to the $^4I_{11/2}$ state of Er^{3+}. Assuming that the ET2 process is dominant to populate the $^4F_{9/2}$ state, then the population of the $^4F_{9/2}$ state n_R can be expressed as

$$n_R = C_{d1} n_d n_1 = C_{d1} n_{d0} n_{10} \exp[-t(1/\tau_d + 1/\tau_1)] \quad (5)$$

where C_{d1} is the coefficient for ET from the $^2F_{5/2}$ state of Yb^{3+} to the $^4I_{13/2}$ state of Er^{3+}. From eqs 4 and 5, the average decay times of the $^2H_{11/2}/^4S_{3/2}$ state $\overline{\tau}_G$ and the $^4F_{9/2}$ state $\overline{\tau}_R$ can be obtained as follows:

$$\overline{\tau}_G = \tau_d \tau_2/(\tau_d + \tau_2) \quad (6)$$

$$\overline{\tau}_R = \tau_d/(\tau_d/\tau_1 + 1) \quad (7)$$

Meanwhile, in a Yb^{3+}- and Er^{3+}-codoped system, the decay time of the $^4I_{13/2}$ state of Er^{3+} τ_1 is much longer than that of the $^2F_{5/2}$ state of Yb^{3+} τ_d; in addition, the decay times of the Yb^{3+}

DOI: 10.1021/acs.inorgchem.9b01229
Inorg. Chem. 2019, 58, 8245−8252

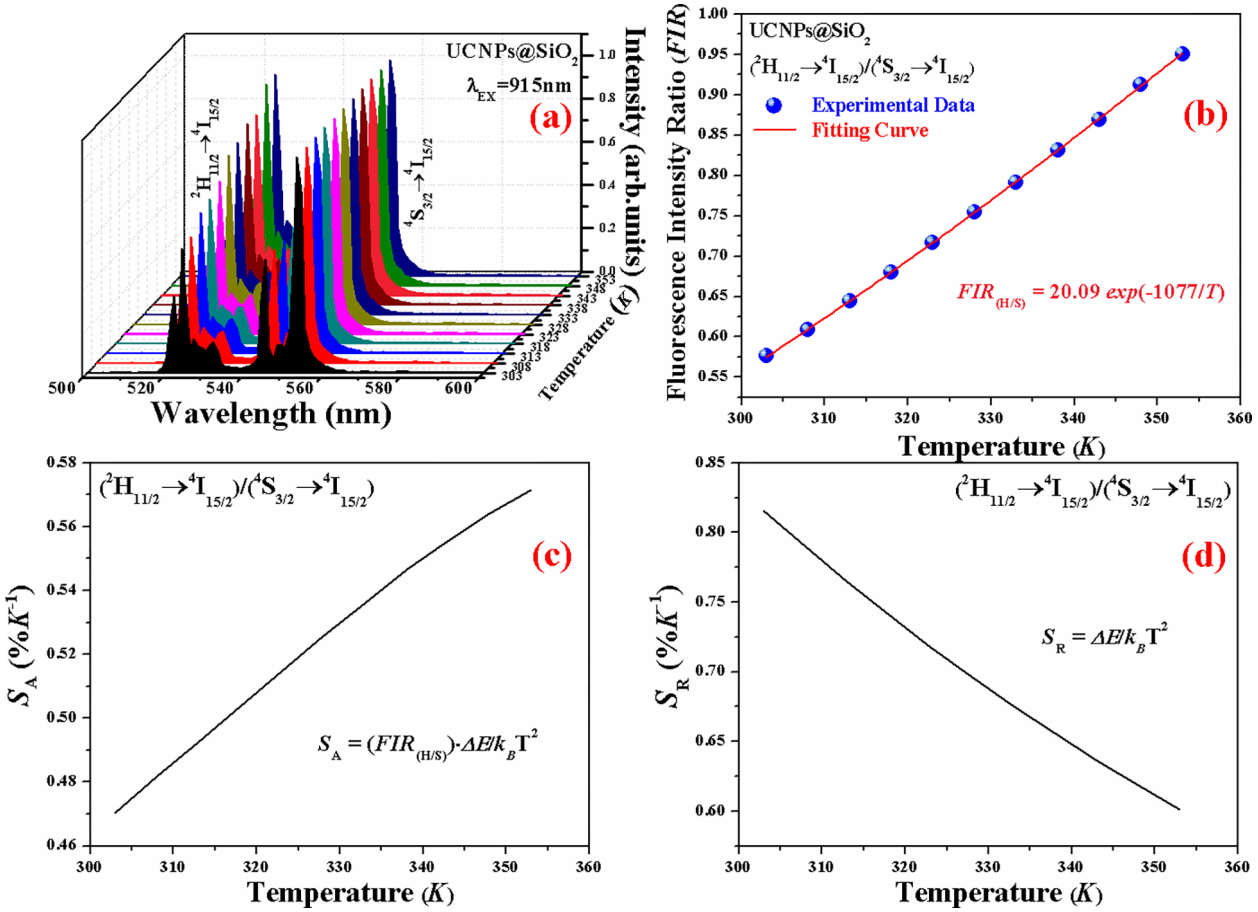

Figure 6. Temperature dependence of (a) UC spectra with the normalized intensities of the $^4S_{3/2} \rightarrow {}^4I_{15/2}$ transition, (b) FIR between the $^2H_{11/2} \rightarrow {}^4I_{15/2}$ and $^4S_{3/2} \rightarrow {}^4I_{15/2}$ transitions, (c) absolute sensitivity S_A, and (d) relative sensitivity S_R in UCNPs@SiO_2 excited by 915 nm wavelength.

$^2F_{5/2}$ state τ_d and Er^{3+} $^4I_{11/2}$ state τ_2 are almost the same, which has been reported previously.[28] Therefore, the average decay times of the $^2H_{11/2}/^4S_{3/2}$ state $\overline{\tau}_G$ and the $^4F_{9/2}$ state $\overline{\tau}_R$ can be expressed as

$$\overline{\tau}_G = \tau_d/2 \tag{6a}$$

$$\overline{\tau}_R = \tau_d \tag{7a}$$

That is to say, the average decay time of the $^2H_{11/2}/^4S_{3/2}$ state is half that of the $^4F_{9/2}$ state, which agrees with the experimental data. In order to further demonstrate the validity of the theory proposed above, the decay curves of the $^2F_{5/2}$ state of Yb^{3+} in each sample were also collected and are depicted in Figure 5c. As can be seen clearly, for each sample, the decay time of the $^2F_{5/2}$ state of Yb^{3+} is almost equal to its corresponding decay time of the $^4F_{9/2}$ state of Er^{3+} and twice the corresponding decay time of the $^2H_{11/2}/^4S_{3/2}$ state of Er^{3+}, which provides potent proof for our theory.

Optical Thermometry Behaviors of UCNPs@SiO$_2$. In order to explore the temperature-sensing properties of UCNPs@SiO_2, the dependences of the UC spectra with temperature in the biological range (303−353 K) under 915-nm-wavelength excitation were recorded and are depicted in Figure 6a. The FIR of the $^2H_{11/2} \rightarrow {}^4I_{15/2}$ and $^4S_{3/2} \rightarrow {}^4I_{15/2}$ transitions changed regularly with increasing temperature (see Figure 6b), resulting from thermal coupling between the $^2H_{11/2}$ and $^4S_{3/2}$ levels of Er^{3+}. The FIR of the $^2H_{11/2} \rightarrow {}^4I_{15/2}$ and $^4S_{3/2} \rightarrow {}^4I_{15/2}$ transitions should follow the equation

$$\mathrm{FIR} = I_H/I_S = g_1\upsilon_1\sigma_1/g_2\upsilon_2\sigma_2 = B\exp(-\Delta E/k_BT) \tag{8}$$

where I is the UC intensity, g, υ, and σ represent the degeneracy degree, spontaneous emission, and absorption rate, respectively. ΔE is the energy gap between $^2H_{11/2}$ and $^4S_{3/2}$, k_B is the Boltzmann constant, and T is the absolute temperature.[29,30] According to eq 8, the fitting of the exponential curves of FIR versus temperature can be written as

$$\mathrm{FIR}_{(H/S)} = 20.09\exp(-1077/T) \tag{9}$$

Utilizing eq 9, we can calculate the energy gap ΔE = 749 cm^{-1}. Meanwhile, the absolute and relative sensitivities (S_A and S_R), which are the key parameters in practical applications, can also be calculated:

$$S_A = |\mathrm{d(FIR)}/\mathrm{d}T| = \mathrm{FIR}(\Delta E/k_BT^2) \tag{10}$$

$$S_R = |\mathrm{d(FIR)}/\mathrm{FIR}\,\mathrm{d}T| = \Delta E/k_BT^2 \tag{11}$$

The curves of S_A and S_R obtained from the above equations are shown in Figure 6c,d. The value of S_A is increased with rising temperature, and the maximum of S_A is 5.72×10^{-3} K^{-1} at 353 K. S_R can be written as $1077/T^2$. Compared with the bare UCNPs, UCNPs@SiO_2 own higher S_A and S_R values (see Figure S1), which is similar to the previous report regarding the temperature-sensing properties of $GdVO_4$:Yb^{3+}/Er^{3+}@SiO_2 NPs.[23] Besides, we also compare the sensitivity of UCNPs@SiO_2 with that of other Yb^{3+}/Er^{3+}-codoped materials for which the FIR of the $^2H_{11/2} \rightarrow {}^4I_{15/2}$ and $^4S_{3/2} \rightarrow {}^4I_{15/2}$ transitions

DOI: 10.1021/acs.inorgchem.9b01229
Inorg. Chem. 2019, 58, 8245−8252

was applied to determine the temperature. As presented in Table 1, whether compared with β-$NaYF_4$:Yb^{3+}/Er^{3+} NPs and β-$NaLuF_4$:Yb^{3+}/Er^{3+} NPs, which are considered to be the most efficient host for UC, or compared with the YVO_4:Yb^{3+}/Er^{3+} NPs, which own structures similar to those of $LuVO_4$ NPs, the UCNPs@SiO_2 in this work displays a higher sensitivity, indicating its potential application for optical thermometry.

Table 1. Values of S_R in Typical Temperature-Sensing Materials Based on FIR between the $^2H_{11/2} \rightarrow {}^4I_{15/2}$ and $^4S_{3/2} \rightarrow {}^4I_{15/2}$ Transitions of Er^{3+}

sensing material	T (K)	S_R (% K^{-1})	ref
$LuVO_4$:Yb^{3+}/Er^{3+}@SiO_2 NPs	303−353	$1077/T^2$	this work
β-$NaLuF_4$:Yb^{3+}/Er^{3+} NPs	295−343	$1073/T^2$	31
$LuVO_4$:Yb^{3+}/Er^{3+} bulk material	303−423	$1030/T^2$	32
α-$NaYF_4$:Yb^{3+}/Er^{3+} NPs		$1028/T^2$	33
YVO_4:Yb^{3+}/Er^{3+} NPs	293−603	$1011/T^2$	34
β-$NaYF_4$:Yb^{3+}/Er^{3+} NPs	298−328	$969/T^2$	35

Beyond that, the temperature dependence of the $^4I_{13/2} \rightarrow {}^4I_{15/2}$ transition under 915-nm-wavelength excitation has also been investigated. As shown in Figure 7a, several emission peaks exist in the range of 1400−1700 nm, which originates from the Stark transitions of the $^4I_{13/2} \rightarrow {}^4I_{15/2}$ transition. More importantly, an anomalous enhancement of the $^4I_{13/2} \rightarrow {}^4I_{15/2}$ transition with increasing temperature is observed, which can be explained as the improvement of the MPR process from the $^4I_{11/2}$ to $^4I_{13/2}$ level at high temperature.[36,37] Consequently, it can be found that the FIR between peak 2 (located at 1496 nm) and peak 1 (located at 1527 nm) regularly changes with the rise of the temperature and can be fitted as follows (see Figure 7b):

$$\mathrm{FIR}_{(P2/P1)} = \exp(-3.6 \times 10^{-6}T^2 + 0.004T - 1.38) \quad (12)$$

The corresponding S_A and S_R were also obtained and are depicted in Figure 7c,d. With a rise of the temperature, the values of S_A and S_R in this case are all decreased. The maximum values of S_A and S_R are 1.09×10^{-3} and 1.82×10^{-3} K^{-1} at 303 K, respectively.

To summarize, under 915-nm-wavelength excitation, in UCNPs@SiO_2, the FIR of the $^2H_{11/2} \rightarrow {}^4I_{15/2}$ transition to the $^4S_{3/2} \rightarrow {}^4I_{15/2}$ transition in the visible region and peak 2 to peak 1 of the $^4I_{13/2} \rightarrow {}^4I_{15/2}$ transition in the IR region can be utilized simultaneously to measure the temperature, which allows for a self-referenced temperature determination to make the measurement of the temperature more precise.

CONCLUSIONS

In conclusion, $LuVO_4$:Yb^{3+}/Er^{3+}@SiO_2 NPs have been demonstrated to own perfect optical thermometry properties under 915-nm-wavelength excitation. In the visible region, S_R for the FIR between the Er^{3+} $^2H_{11/2}$ level and the $^4S_{3/2}$ level can be written as $1077/T^2$, which is higher than that of β-

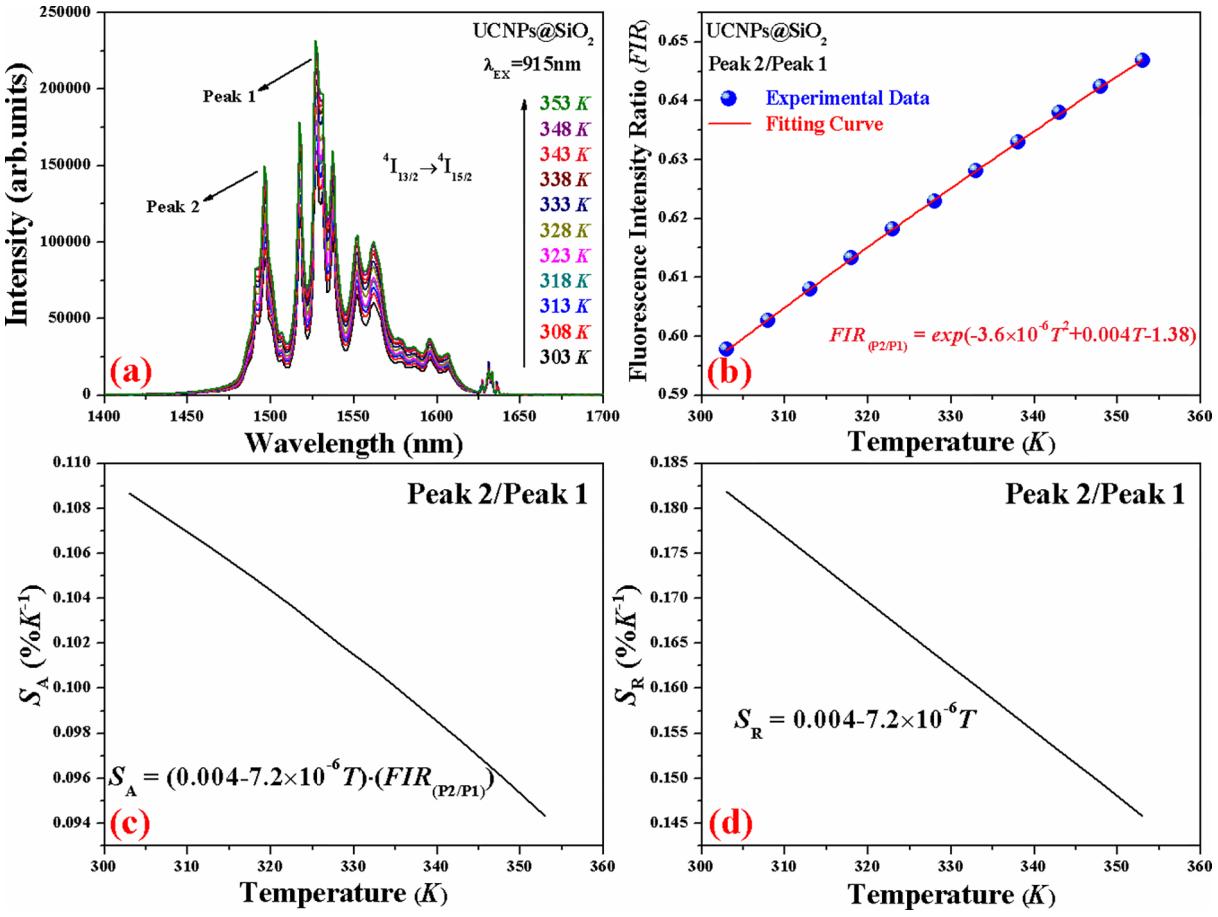

Figure 7. Temperature dependence of (a) the $^4I_{13/2} \rightarrow {}^4I_{15/2}$ transition, (b) FIR between peak 2 (at 1496 nm) and peak 1 (at 1527 nm), and (c) S_A and (d) S_R in UCNPs@SiO_2 under 915-nm-wavelength excitation.

DOI: 10.1021/acs.inorgchem.9b01229
Inorg. Chem. 2019, 58, 8245−8252

$NaYF_4$:Yb^{3+}/Er^{3+} NPs, β-$NaLuF_4$:Yb^{3+}/Er^{3+} NPs, YVO_4:Yb^{3+}/Er^{3+} NPs, etc. In the NIR region, an anomalous enhancement of the $^4I_{13/2} \rightarrow {}^4I_{15/2}$ transition with increasing temperature is observed, resulting from the enhancement of the MPR process from the $^4I_{11/2}$ to $^4I_{13/2}$ level at high temperature. What is more, the FIR between peak 2 (located at 1496 nm) and peak 1 (located at 1527 nm) is changed regularly with increasing temperature, which can be used to measure the temperature. The simultaneous utilization of the two methods for optical thermometry can provide a self-referenced temperature determination to make measurement of the temperature more precise. Moreover, by using a SiO_2 coating, the UC intensity of the NPs is dramatically increased. In addition, the UC mechanism, especially the population route of the Er^{3+} $^4F_{9/2}$ level, is studied in detail. Through analysis of the decay curves, we propose that the dominant way for populating the Er^{3+} $^4F_{9/2}$ level is ET from the Yb^{3+} $^2F_{5/2}$ level to the Er^{3+} $^4I_{13/2}$ level. The excellent UC and optical thermometry properties under 915-nm-wavelength excitation make it possible to use the NPs for biological applications, such as optical thermometry, bioimaging, PDT, etc.

■ ASSOCIATED CONTENT

Supporting Information

The Supporting Information is available free of charge on the ACS Publications website at DOI: 10.1021/acs.inorgchem.9b01229.

Temperature dependence of the UC spectra, FIR, and S_A and S_R in UCNPs (PDF)

■ AUTHOR INFORMATION

Corresponding Author

*E-mail: xianggt@cqupt.edu.cn (G.X.).

ORCID

Guotao Xiang: 0000-0003-3587-6654

Xianju Zhou: 0000-0002-8050-9688

Li Li: 0000-0003-1163-5733

Notes

The authors declare no competing financial interest.

■ ACKNOWLEDGMENTS

This work is financially supported by National Natural Science Foundation of China (Grants 11674044, 11604037, and 11704054), Chongqing Research Program of Basic Research and Frontier Technology (Grants CSTC2016jcyjA0113 and CSTC2017jcyjAX0046), and Science and Technology Research Program of Chongqing Municipal Education Commission (Grant KJZD-K201800602).

■ REFERENCES

(1) Mukhopadhyay, L.; Rai, V. K.; Bokolia, R.; Sreenivas, K. 980 nm excited Er^{3+}/Yb^{3+}/Li^+/Ba^{2+}: $NaZnPO_4$ upconverting phosphors in optical thermometry. *J. Lumin.* **2017**, *187*, 368−377.

(2) Gao, Y.; Huang, F.; Lin, H.; Zhou, J. C.; Xu, J.; Wang, Y. S. A Novel Optical Thermometry Strategy Based on Diverse Thermal Response from Two Intervalence Charge Transfer States. *Adv. Funct. Mater.* **2016**, *26*, 3139−3145.

(3) Du, P.; Luo, L. H.; Park, H. K.; Yu, J. S. Citric-assisted sol-gel based Er^{3+}/Yb^{3+}-codoped $Na_{0.5}Gd_{0.5}MoO_4$: A novel highly-efficient infrared-to-visible upconversion material for optical temperature sensors and optical heaters. *Chem. Eng. J.* **2016**, *306*, 840−848.

(4) Wu, Y. F.; Suo, H.; He, D.; Guo, C. F. Highly sensitive up-conversion optical thermometry based on Yb^{3+}-Er^{3+} codoped $NaLa(MoO_4)_2$ green phosphors. *Mater. Res. Bull.* **2018**, *106*, 14−18.

(5) Suo, H.; Zhao, X. Q.; Zhang, Z. Y.; Wu, Y. F.; Guo, C. F. Upconverting $LuVO_4$:Nd^{3+}/Yb^{3+}/Er^{3+}@SiO_2@Cu_2S Hollow Nanoplatforms for Self-monitored Photothermal Ablation. *ACS Appl. Mater. Interfaces* **2018**, *10*, 39912−39920.

(6) Gao, Y.; Cheng, Y.; Hu, T.; Ji, Z. L.; Lin, H.; Xu, J.; Wang, Y. S. Broadening the valid temperature range of optical thermometry through dual-mode design. *J. Mater. Chem. C* **2018**, *6*, 11178−11183.

(7) Cheng, Y.; Gao, Y.; Lin, H.; Huang, F.; Wang, Y. S. Strategy design for ratiometric luminescence thermometry: circumventing the limitation of thermally coupled levels. *J. Mater. Chem. C* **2018**, *6*, 7462−7478.

(8) Zhang, Y.; Chai, X. N.; Li, J.; Wang, X. S.; Li, Y. X.; Yao, X. Enhanced up-conversion luminescence and excellent temperature sensing properties in Yb^{3+} sensitized Er^{3+}-doped $Bi_3Ti_{1.5}W_{0.5}O_9$ multifunctional ferroelectric ceramics. *J. Alloys Compd.* **2018**, *735*, 473−479.

(9) Du, P.; Luo, L. H.; Huang, X. Y.; Yu, J. S. Ultrafast synthesis of bifunctional Er^{3+}/Yb^{3+}-codoped $NaBiF_4$ upconverting nanoparticles for nanothermometer and optical heater. *J. Colloid Interface Sci.* **2018**, *514*, 172−181.

(10) Cao, J. K.; Chen, W. P.; Xu, D. K.; Hu, F. F.; Chen, L. P.; Guo, H. Wide-range thermometry based on green up-conversion of Yb^{3+}/Er^{3+} codoped KLu_2F_7 transparent bulk oxyfluoride glass ceramics. *J. Lumin.* **2018**, *194*, 219−224.

(11) Liu, Y. J.; Lu, Y. Q.; Yang, X. S.; Zheng, X. L.; Wen, S. H.; Wang, F.; Vidal, X.; Zhao, J. B.; Liu, D. M.; Zhou, Z. G.; Ma, C. S.; Zhou, J. J.; Piper, J. A.; Xi, P.; Jin, D. Y. Amplified stimulated emission in upconversion nanoparticles for super-resolution nanoscopy. *Nature* **2017**, *543*, 229−233.

(12) Chen, S.; Weitemier, A. Z.; Zeng, X.; He, L. M.; Wang, X. Y.; Tao, Y. Q.; Huang, A. J. Y.; Hashimotodani, Y.; Kano, M.; Iwasaki, H.; Parajuli, L. K.; Okabe, S.; Teh, D. B. L.; All, A. H.; Tsutsui-Kimura, I.; Tanaka, K. F.; Liu, X. G.; McHugh, T. J. *Science* **2018**, *359*, 679−684.

(13) Wang, F.; Wen, S. H.; He, H.; Wang, B. M.; Zhou, Z. G.; Shimoni, O.; Jin, D. Y. Microscopic inspection and tracking of single upconversion nanoparticles in living cells. *Light: Sci. Appl.* **2018**, *7*, e18007.

(14) Yao, C.; Wang, W. X.; Wang, P. Y.; Zhao, M. Y.; Li, X. M.; Zhang, F. Near-Infrared Upconversion Mesoporous Cerium Oxide Hollow Biophotocatalyst for Concurrent pH-/H_2O_2-Responsive O_2-Evolving Synergetic Cancer Therapy. *Adv. Mater.* **2018**, *30*, 1704833.

(15) Kou, L.; Labrie, D.; Chylek, P. Refractive indices of water and ice in the 0.65- to 2.5-μm spectral range. *Appl. Opt.* **1993**, *32*, 3531−3540.

(16) Lu, F.; Yang, L.; Ding, Y. J.; Zhu, J. J. Highly Emissive Nd^{3+}-Sensitized Multilayered Upconversion Nanoparticles for Efficient 795 nm Operated Photodynamic Therapy. *Adv. Funct. Mater.* **2016**, *26*, 4778−4785.

(17) Xu, B.; Zhang, X.; Huang, W. J.; Yang, Y. J.; Ma, Y.; Gu, Z. J.; Zhai, T. Y.; Zhao, Y. L. Nd^{3+} sensitized dumbbell-like upconversion nanoparticles for photodynamic therapy application. *J. Mater. Chem. B* **2016**, *4*, 2776−2784.

(18) Huang, Ya. N.; Xiao, Q. B.; Hu, H. S.; Zhang, K. C.; Feng, Y. M.; Li, F. J.; Wang, J.; Ding, X. G.; Jiang, J.; Li, Y. F.; Shi, L. Y.; Lin, H. Z. 915 nm Light-Triggered Photodynamic Therapy and MR/CT Dual-Modal Imaging of Tumor Based on the Nonstoichiometric $Na_{0.52}YbF_{3.52}$: Er Upconversion Nanoprobes. *Small* **2016**, *12*, 4200−4210.

(19) Zhan, Q. Q.; Qian, J.; Liang, H. J.; Somesfalean, G.; Wang, D.; He, S. L.; Zhang, Z. G.; Andersson-Engels, S. Using 915 nm Laser Excited Tm^{3+}/Er^{3+}/Ho^{3+}-Doped $NaYbF_4$ Upconversion Nanoparticles for in Vitro and Deeper in Vivo Bioimaging without Overheating Irradiation. *ACS Nano* **2011**, *5*, 3744−3757.

(20) Cheng, F. M.; Sun, K. N.; Zhao, Y.; Liang, Y. J.; Xin, Q.; Sun, X. L. Synthesis and characterization of HA/YVO_4: Yb^{3+}, Er^{3+} up-

DOI: 10.1021/acs.inorgchem.9b01229
Inorg. Chem. 2019, 58, 8245−8252

conversion luminescent nano-rods. *Ceram. Int.* **2014**, *40*, 11329−11334.
(21) Oh, J. H.; Moon, B. K.; Choi, B. C.; Jeong, J. H.; Kim, J. H.; Lee, H. S. The green upconversion emission mechanism investigation of $GdVO_4$:Yb^{3+}, Er^{3+} via tuning of the sensitizer concentration. *Solid State Sci.* **2015**, *42*, 1−5.
(22) Zhao, S.; Tian, R. R.; Shao, B. Q.; Feng, Y.; Yuan, S. W.; Dong, L. P.; Zhang, L.; Liu, K.; Wang, Z. X.; You, H. P. Designing of UCNPs@Bi@SiO_2 Hybrid Theranostic Nanoplatforms for Simultaneous Multimodal Imaging and Photothermal Therapy. *ACS Appl. Mater. Interfaces* **2019**, *11*, 394−402.
(23) Savchuk, O. A.; Carvajal, J. J.; Cascales, C.; Aguiló, M.; Díaz, F. Benefits of Silica Core−Shell Structures on the Temperature Sensing Properties of Er,Yb:$GdVO_4$ Up-Conversion Nanoparticles. *ACS Appl. Mater. Interfaces* **2016**, *8*, 7266−7273.
(24) Zhao, R. F.; Wu, Q. H.; Tang, D. M.; Li, W. L.; Zhang, X.; Chen, M.; Guo, R.; Diao, G. W. Double-shell CeO_2:Yb, Er@SiO_2@Ag upconversion composite nanofibers as an assistant layer enhanced near-infrared harvesting for dye-sensitized solar cells. *J. Alloys Compd.* **2018**, *769*, 92−95.
(25) Nien, Y. T.; Chen, K. M.; Chen, I. G. Improved Photoluminescence of $Y_3Al_5O_{12}$:Ce Nanoparticles by Silica Coating. *J. Am. Ceram. Soc.* **2010**, *93*, 1688−1691.
(26) Calderón-Villajos, R.; Zaldo, C.; Cascales, C. Enhanced upconversion multicolor and white light luminescence in SiO_2-coated lanthanide-doped $GdVO_4$ hydrothermal nanocrystals. *Nanotechnology* **2012**, *23*, 505205.
(27) Xiang, G. T.; Zhang, J. H.; Hao, Z. D.; Zhang, X.; Pan, G. H.; Luo, Y. S.; Lü, W.; Zhao, H. F. Importance of Suppression of Yb^{3+} De-Excitation to Upconversion Enhancement in β-$NaYF_4$: Yb^{3+}/Er^{3+}@β-$NaYF_4$ Sandwiched Structure Nanocrystals. *Inorg. Chem.* **2015**, *54*, 3921−3928.
(28) Liu, L. X.; Qin, F.; Zhao, H.; Lv, T. Q.; Zhang, Z. G.; Cao, W. W. Shell thickness dependence of upconversion luminescence of β-$NaYF_4$:Yb, Er/β-$NaYF_4$ core-shell nanocrystals. *Opt. Lett.* **2013**, *38*, 2101−2103.
(29) Jiang, S.; Zeng, P.; Liao, L. Q.; Tian, S. F.; Guo, H.; Chen, Y. H.; Duan, C. K.; Yin, M. Optical thermometry based on upconverted luminescence in transparent glass ceramics containing $NaYF_4$:Yb^{3+}/Er^{3+} nanocrystals. *J. Alloys Compd.* **2014**, *617*, 538−541.
(30) Suo, H.; Guo, C. F.; Li, T. Broad-Scope Thermometry Based on Dual-Color Modulation up-Conversion Phosphor $Ba_5Gd_8Zn_4O_{21}$:Er^{3+}/Yb^{3+}. *J. Phys. Chem. C* **2016**, *120*, 2914−2924.
(31) Li, D. Y.; Tian, L. L.; Huang, Z.; Shao, L. X.; Quan, J.; Wang, Y. X. Optical Temperature Sensor Based on Infrared Excited Green Upconversion Emission in Hexagonal Phase $NaLuF_4$:Yb^{3+}/Er^{3+} Nanorods. *J. Nanosci. Nanotechnol.* **2016**, *16*, 3641−3645.
(32) Ma, Y.; Xiang, G. T.; Zhang, J. H.; Liu, Z.; Zhou, P.; Liu, W.; Tang, X.; Jiang, S.; Zhou, X. J.; Li, L.; Luo, Y. S.; Jin, Y. Upconversion properties and temperature sensing behaviors in visible and near-infrared region based on fluorescence intensity ratio in $LuVO_4$: Yb^{3+}/Er^{3+}. *J. Alloys Compd.* **2018**, *769*, 325−331.
(33) Vetrone, F.; Naccache, R.; Zamarrón, A.; Juarranz de la Fuente, A.; Sanz-Rodríguez, F.; Martinez Maestro, L.; Martín Rodriguez, E.; Jaque, D.; Garcia Solé, J.; Capobianco, J. A. Temperature Sensing Using Fluorescent Nanothermometers. *ACS Nano* **2010**, *4*, 3254−3258.
(34) Meng, Q. Y.; Liu, T.; Dai, J. Q.; Sun, W. J. Study on optical temperature sensing properties of YVO_4:Er^{3+}, Yb^{3+} nanocrystals. *J. Lumin.* **2016**, *179*, 633−638.
(35) Huo, L. L.; Zhou, J. J.; Wu, R. Z.; Ren, J. F.; Zhang, S. J.; Zhang, J. J.; Xu, S. Q. Dual-functional β-$NaYF_4$: Yb^{3+}, Er^{3+} nanoparticles for bioimaging and temperature sensing. *Opt. Mater. Express* **2016**, *6*, 1056−1064.
(36) Yuan, N.; Liu, D. Y.; Yu, X. C.; Sun, H. X.; Ming, C. G.; Wong, W. H.; Song, F.; Yu, D. Y.; Pun, E. Y. B.; Zhang, D. L. A biological nano-thermometer based on ratiometric luminescent Er^{3+}/Yb^{3+}-codoped $NaGd(WO_4)_2$ nanocrystals. *Mater. Lett.* **2018**, *218*, 337−340.
(37) Yu, D.; Ballato, J.; Riman, R. E. Temperature-Dependence of Multiphonon Relaxation of Rare-Earth Ions in Solid-State Hosts. *J. Phys. Chem. C* **2016**, *120*, 9958−9964.

DOI: 10.1021/acs.inorgchem.9b01229
Inorg. Chem. 2019, 58, 8245−8252